Electronic Supplementary Material (ESI) for Physical Chemistry Chemical Physics
This journal is © The Owner Societies 2011

Zeolite Y and A Crystallization Compared by Simultaneous UV/VIS-Raman and X-Ray Diffraction

Anouschka Depla, Elke Verheyen, An Veyfeyken, Elena Gobechiya, Thomas Hartmann, Reinhold Schaefer, Johan A. Martens and Christine E. A. Kirschhock *

Supplementary Data

Combined Raman and XRD setup

To successfully design a flexible setup combining XRD and Raman several ancillary conditions had to be respected. Main requirement was the continuous accessibility of the sample position for both optical paths, while access of the sample for sample exchange or change of the sample environment should not be hindered. The most obvious solution was one permanently fixed sample position. A second important requirement was to achieve the highest possible flexibility for both techniques. Allowing for the implementation of different diffraction geometries, i.e. Bragg-Brentano geometry (reflection mode), Transmission (Debye Scherrer for capillaries) and High Flux (focusing the beam on the sample), limited the choices for the diffraction optics. Excellent resolution can be achieved by using a focussed beam optics, preferably using Kα1 only. This is done by using a curved Ge 111 monochromator. However, contrary to diffraction optics relying on a parallel beam, different diffraction geometries in focussed configuration depend on variation of sample–detector distances to ensure focus of the diffracted signals on the detector plane. By fixing the sample position the only solution was to implement a flexible positioning of the X-ray tube, including monochromator. This demand was fullfilled by redesign of a diffractometer, available on the market, but depending on a flexible sample position (STADI MP by STOE & Cie GmbH). A rail system was conceived which allowed easy change of tube position to switch between diffraction geometries without the need to realign the X-ray path and allowing fixation of sample position. With the X-ray tube in position 1, a convergent beam is focussed through the sample on the PSD. The diffracted signals are focussed on the detector plane, too (Fig. 1). A tube in this position is ideal for capillary and transmission measurements yielding excellent resolution. With position 2 the beam is focussed on a minimum sample area for microdiffraction and laterally resolved studies, like texture- and

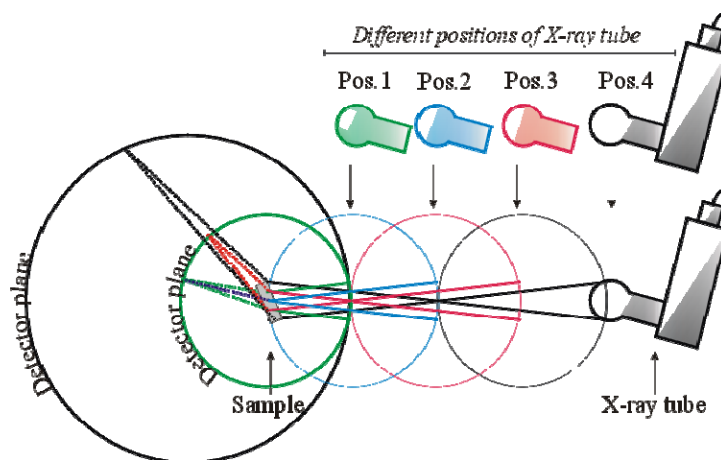

Fig. 1: Three accessible X-ray geometries by a movable X-ray tube to increase the sample to X-ray tube distance: Transmission (Pos.1), High flux mode (Pos. 2) and Bragg-Brentano reflection mode (Pos.3: low resolution; Pos.4: high resolution)

stress analysis. Positions 3 and 4 make use of the refocussing during reflection on the sample in Bragg-Brentano configuration (Fig. 1). Due to the increased source-to-sample distance in position 4, the reflected signals result in higher resolution, as the detector records a smaller part of the 2θ circle. As combined diffraction-Raman studies were foreseen not only for solid samples but also for liquids and gels on the verge of crystallization a horizontal sample position in Bragg-Brentano geometry was a further requirement to ensure a flat and stable sample surface. This left as only option a vertical diffractometer arrangement, which immediately defined the vertical plane as detection plane for the diffraction (Fig. 2 and 3).

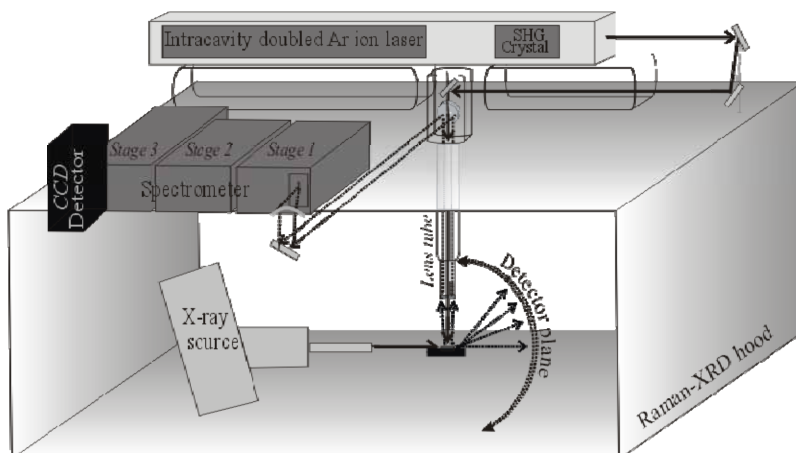

Fig. 2: Back side view on the Raman-XRD setup with detailed optical Raman and XRD paths of sample radiation (solid lines) and scattered signal collection (dashed lines).

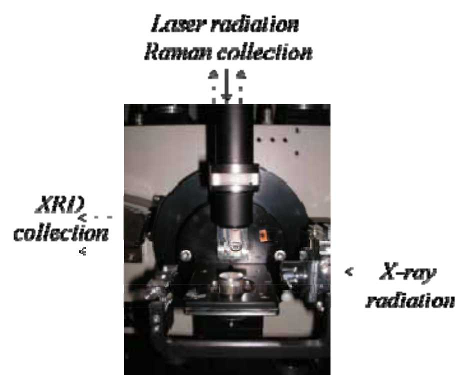

Fig. 3: The optical paths for Raman and XRD radiation (solid lines) and collection (dashed lines).

stress analysis. Positions 3 and 4 make use of the refocussing during reflection on the sample in Bragg-Brentano configuration (Fig. 1). Due to the increased source-to-sample distance in position 4, the reflected signals result in higher resolution, as the detector records a smaller part of the 2θ circle. As combined diffraction-Raman studies were foreseen not only for solid samples but also for liquids and gels on the verge of crystallization a horizontal sample position in Bragg-Brentano geometry was a further requirement to ensure a flat and stable sample surface. This left as only option a vertical diffractometer arrangement, which immediately defined the vertical plane as detection plane for the diffraction (Fig. 2 and 3). With this, the only possible option for access of the sample by Raman excitation and collection remained the upper hemisphere around the sample. A vertical incidence of the laser beam and collection of Raman signals in backscattering was selected (Fig. 3).

Besides optimization of the XRD setup, the Raman optics were chosen to reach the highest performance. To take advantage of Resonance Raman effects and to avoid recurrent problems of fluorescence, UV excitation was chosen asides the option of also using visible light. As no UV fiber optics with sufficient quality were available on the market the optical Raman path was designed using mirrors and lenses. To reduce losses, the path was minimized which led to mounting of both laser and spectrometer on top of the specially enforced diffractometer hood. The hood also serves as radiation protection and for exclusion of stray light. In addition to the flexibility of the combined optical paths, this arrangement of the individual components also led to the highly appreciated side effect of simple sample access from the front of the machine. Depending on the sample properties, different sample holders are available: open flat discs for thin films, shallow curved discs for powders or liquids and sealed capillaries for air-sensitive samples.

To implement this demanding plan in practice, a close collaboration with industry was mandatory for both optical paths and the specific custom requirements. Collaboration on the XRD and Raman part was established with STOE & Cie GmbH and S&I Spectroscopy & Imaging GmbH, respectively. The intensive collaboration led to the development of the combined XRD-Raman instrument, visualized in Fig. 4. The radiation protection hood of the custom made STADI Multi-Purpose X-ray diffractometer (STOE & Cie GmbH) encloses sample environment (c), CuKα X-ray tube (λ = 1.54056 Å) (b), asymmetric Ge (111) monochromator and the position sensitive detector (d) (Fig. 4). Currently, the machine is equipped with a linear position sensitive detector (PSD), essential for high resolutions and structure refinement studies (Fig. 3). A number of other X-ray detectors can easily be installed in the combined setup. A curved image plate detector (curved IP-PSD) for fast and high intensity patterns of rapidly evolving systems is among the possibilities (Fig. 3). The carefully conceived Raman part, installed on top of the hood (Fig. 4), contains the following individual instruments: a Coherent Innova 300C MotoFred Ar-ion laser (a), a S&I Spectroscopy & Imaging GmbH Trivista TR557 A&S triple-stage spectrometer (e) and a liquid nitrogen cooled back-illuminated CCD camera (Princeton Instruments) (f). The laser has access to two fundamental wavelengths in the visible region, 488 and 514 nm, with output powers of 1.5 and 2 W respectively. These lines are optionally frequency doubled by the use of a nonlinear crystal, BBO (β-barium borate, BaB_2O_4), to produce two additional UV lines (244 and 257 nm). The UV-output power of the laser is 0.1 W. The three coupled spectrometer stages all have Czerny-turner configuration and motorized grating turets with three different gratings. The grating choice mainly depends on the desired spectroscopic resolution. Detailed specifications of all gratings are provided in the Supplementary Data. The spectrometer stages have focal lengths of 500, 500 and 750 mm respectively. The dispersion power of the three stages are normally added to promote ultra-high resolution. The increased length of the last stage further enhances spectral resolution (FWHM) to ~ 1.4 and ~ 0.4 cm^{-1} for 244 and 514 nm, respectively, with added and entrance slit width of 13 μm. Not only high resolution, but also a close Rayleigh approach is mandatory in several cases.

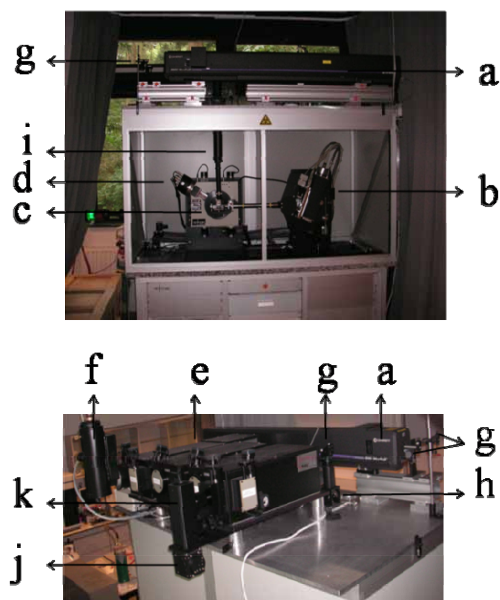

Fig. 4: DiffRam front view (top) and back side view from the top (bottom). Components: Ar- ion laser (a), X-ray tube (b), sample environment (c), X-ray detector (d), spectrometer (e), CCD detector (f), reflection mirrors (g), Al mirror with hole (h), tube with UV grade lens (i), Al mirror (j), parabolic mirror (k).

In silica growth processes f.e., it is crucial to record the low frequency vibrations of the different silicate species in solution. For this, the spectrometer additionally offers the possibility to use the stages in a substractive mode. The first two stages now act as a Rayleigh filter, while only the last stage disperses the light. The switch between high resolution recordings or extreme Rayleigh approach (below ~ 30 cm^{-1}) is fully automated and controlled by the software. After dispersion, Raman spectra are recorded by a liquid nitrogen cooled back-illuminated CCD camera. This type of detector, known for its high performance and low noise recordings, is mandatory in the analysis of low Raman scatterers, like most inorganic materials.

The choice for a UV laser source and the positioning of the Raman components in the upper hemisphere of the sample environment, greatly encumbered the construction of the optical Raman path. Currently, the laser beam is guided to the sample by three reflecting dielectric mirrors (g), a protected Al mirror with hole for laser throughput (h) and a focussing TGS1 lens (i) (Fig. 4). The type of reflecting mirrors is adapted to the laser line in use. Detailed optical specifications of all optical components in use are provided in the Supplementary Data. The focussing and collecting lens is mounted in a lens tube (i in Fig. 4) with precision screws for both, optimalization of the focal point and XY-positioning of the spot. After the

laser excited the sample, Raman scattering is collected by the same lens in back-scattering geometry. The signal is further directed and focussed on to the spectrometer entrance (e) by subsequent use of the mirror with a hole (h), an enhanced Al mirror (j) and a parabolic 90° off-axis mirror with 152.4 mm focal length (k) (Fig. 4). The hole in the mirror additionally serves as a filter for laser light directly reflected on the sample surface.

In a previous setup, laser focus and collection was not performed in backscattering configuration by a lens, but in a 45° off-axis configuration by a parabolic Al mirror (Newport). This was initially conceived, as the corresponding 45° off-axis approach, allowed wider X-ray detector movements between -80° and 140° 2θ. The setup gave excellent Raman and XRD results, except for the 244 nm Raman line. The signal to noise ratio extremely decreased over a short period of time. Apparently, the noise originated from a degradation of the UV-protective coating of the parabolic mirror. Two different parabolic mirrors gave the same problem. To circumvent the problem, a high quality UV lens (Lambda Research Optics, Inc.) was chosen. This urged a re-configuration of the Raman path from a 45° off axis angle to the current backscattering setup. With this modification, the DiffRam is now fully operational and Raman performance is even improved due to the backscattering geometry. The only downside of the current setup lies in a restriction of the upper range of the X-ray detector movement due to the on-axis localization of the lens tube. For simultaneous studies, the upper limit of the X-ray detector is now limited to 80° instead of 140° 2θ. Actually, this is no serious limitation in the monitoring of fast evolving transitions in material growth processes or deformation studies, because in most cases only a limited angle range needs to be monitored to assess the evolution of crystallinity. Nevertheless, it's highly important to have access to the full 2θ range in the last stage of the crystalline growth process. For this, the lens tube can easily be removed and remounted, to allow access to the full 2θ range for X-ray measurements.

Detailed specifications of all optical components:

All optical components in use have surface flatness of λ/10 and surface quality of 10/5 SD. For further specifications they are devided into the laser-to-sample path and the sample-to-

This journal is © The Owner Societies 2011

spectrometer path.

Optics on the path from laser to sample:

- The type of the three reflection mirrors depend on the laser line in use: Typical Ar-ion laser mirrors for UV and broadband mirrors for VIS applications. All are dielectric and 25.4 mm with a UV grade fused silica substrate and average reflectivity of >99 % (Thorlabs).
- The mirror with the hole for laser througput is a custom made 50.8 mm protected Aluminum mirror with a SiO_2 coating (Bernhard Halle Nachfolger GmbH).
- The focussing and collecting lens is a 25.4 mm UV grade fused silica lens with 50 mm focal length (Lambda Research Optics, Inc.).
- Optics on the path from sample to spectrometer:
- The mirror with the hole is a custom made 50.8 mm protected Aluminum mirror with a SiO_2 coating (Bernhard Halle Nachfolger GmbH).
- An enhanced Al mirror with MGF2 coating (50.8 mm, Edmund Optics)
- a parabolic 90° off-axis Al mirror with SiO_2 coating and 152.4 mm focal length (50.8 mm, Edmund Optics)

Detailed specifications of all gratings:

The available gratings have 300, 500, 900, 1800 or 3600 grooves/mm. The grating types and blaze wavelengths are listed below:

- 300 gr/mm, ruled, blazed at 500 nm (250 nm in 2nd order)
- 500 gr/mm, ruled, blazed at 560 nm (280 nm in 2nd order)
- 900 gr/mm, ruled, blazed at 550 nm (275 nm in 2nd order)
-1800 gr/mm, High Modulation Holographic, optimized for 350 to 800 nm (can be used in 2nd order between 200 and 400 nm)
- 3600 gr/mm, ruled, blazed at 240 nm

This journal is © The Owner Societies 2011

Raman-XRD signatures of the final zeolite X and A powders

The pattern of the final zeolite X powder contained the typical XRD and Raman signatures of FAU topology. The Raman pattern showed the symmetrical T-O stretch at 775 cm^{-1} and asymetrical stretch ~ 960, 1040 and 1085 cm^{-1}. The typical breathing vibration of 4- (515 and 465 cm^{-1}) and 6-rings (290 and 380 cm^{-1}) are present. Some small impurities of zeolite A do occur in the diffraction pattern of zeolite X. Rietveld refinement defined the impurty to be lower than 5% . The impurity in the X zeolite is apparent to low to influence the UV-Raman spectroscopic signature (Fig. 5). For a profound study of the synthesis process, a further increase in the purity of zeolite X during synthesis seems meaningful.

The pattern of the final zeolite A powder contained the typical XRD and Raman signatures of LTA topology. Raman revealed the typical low frequency vibrations, which were already present in the last stages of the crystallization process (280, 340, 410 and 490 cm^{-1}). Additionally, the symmetrical T-O stretch at 695, 740 and 840 cm^{-1} and the asymetrical stretch at 965, 1040 and 1095 cm^{-1} are present.

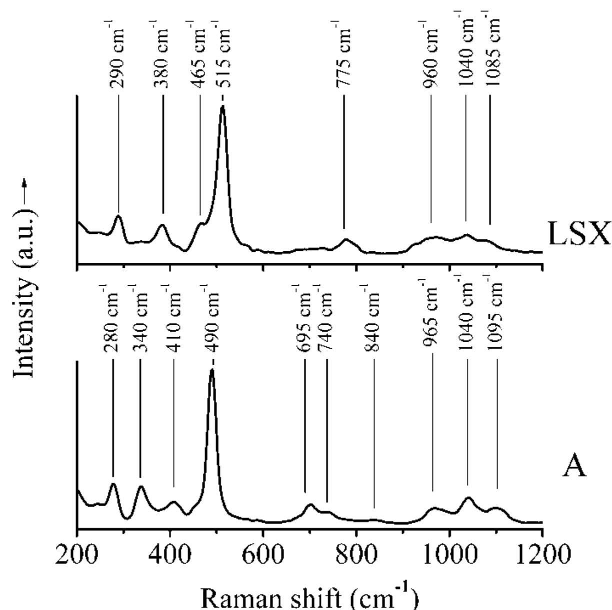

Fig. 5: UV-Raman spectra of the final Low-Silica X (top) and A zeolite powder (bottom).

This journal is © The Owner Societies 2011

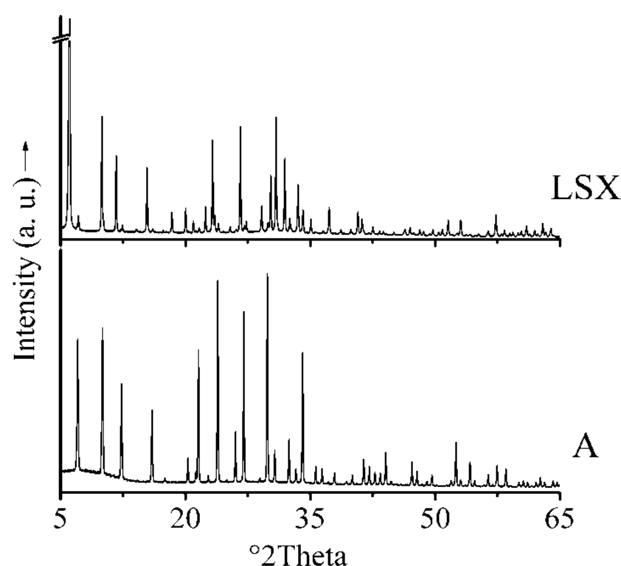

Fig. 6: XRD pattern of the final Low-Silica X (top) and A zeolite powder (bottom).

Raman signatures of the liquid phase during zeolite X and A synthesis

Investigation of the vibrational Raman signature of the liquid phase in the hydrothermal synthesis of zeolite X and A. The liquid phases of both materials are characterized by vibrations at ~ 480, 620, 730, 770, 920 cm^{-1}. The first vibration corresponds to amorphous silicate and 620 cm^{-1} vibration originate from $Al(OH)_4^-$ species. The vibrations ~ 770 and 920 cm^{-1} are assigned in literature to monomeric and even larger oligomeric species, which might originated from a depolymerization of the gel. They were reported in zeolite X synthesis from seeds solution to initially increase in time and afterwards decreased again. UV-Raman monitoring of the liquid phase during the synthesis of both zeolites revealed no major vibrational changes in the bands around 770 and 920 cm^{-1}. Although, a similar behavior as reported for the 770 and 920 cm^{-1} vibrations, might be observed for the 730 cm^{-1} vibration in zeolite X synthesis. For both zeolites, apparently also no major changes occur in the 620 cm^{-1} vibration. The observed lack of major vibrational changes, was previously observed by Dutta and Shieh on zeolite A crystallization departing from an aluminosilicate gel.

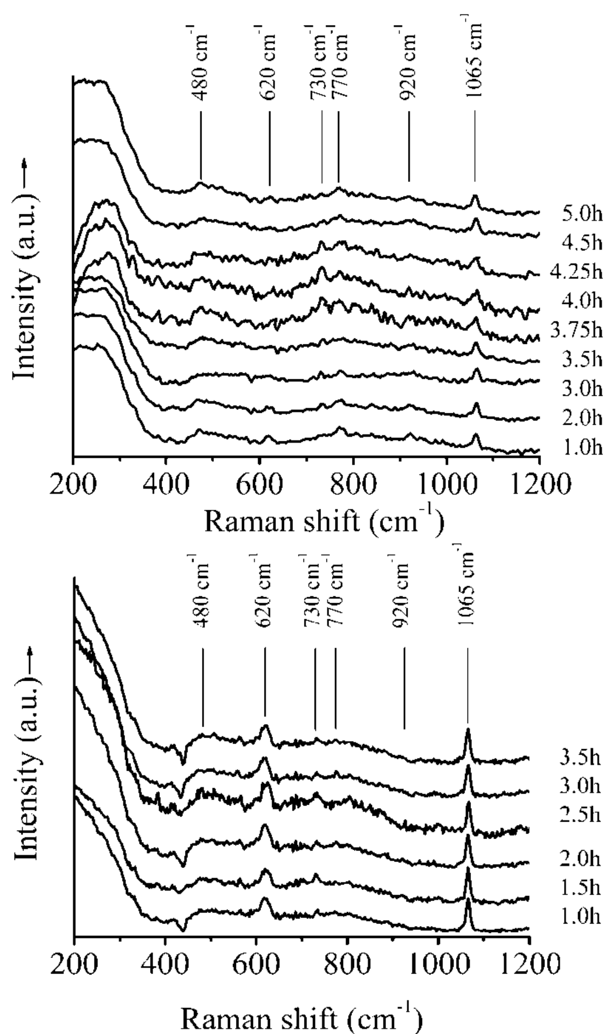

Fig. 7 : UV-Raman spectra of the liquid phase during the hydrothermal condensation of Low-Silica X (top) and A zeolite (bottom).

Raman signatures of the *in situ* crystallization of zeolite A synthesis at 4 h together with the separate solid and liquid phases.

The DiffRam recorded with success simultaneous UV-Raman spectra and XRD patterns from an *in situ* sample of 4 h in the crystallization process of Zeolite A. The *in situ* XRD diffractograms, taken at 4 h (Fig. 6), clearly confirmed the presence of zeolite A crystals evidenced by the characteristic diffractions between 5° and 15° 2θ. The simultaneous *in situ* UV-Raman spectra are given in Fig. 6 together with the separate Raman recordings of both the solid and liquid phase. These were separated by a centrifugation step prior to recording.

The zeolite A crystals formed in the solid phase exhibited the typical bending vibrations of 4- (490 cm^{-1}) and 6-rings (280, 340 and 410 cm^{-1}) next to the symmetrical (700 and 770 cm^{-1}) and asymetrical (1040, 1065 and 1095 cm^{-1}) T-O stretch.[1-6] The surrounding liquid is characterized by vibrations around 620, 730, 770 and 920 cm^{-1} and 1065 cm^{-1}. The vibrations originate from $Al(OH)_4^-$ species (620 cm^{-1}) and monomeric or even larger oligomeric species in solution (~ 770 and 920 cm^{-1}).[7-10] Both the signatures of solid and liquid phase are present in the *in situ* UV-Raman spectra and XRD patterns, although all Raman and XRD patterns have a somewhat lowered intensity. This is quite normal due to the dilution effect caused by the contribution of scattering from both the solid and liquid phase in *in situ* samples. Apparent, the DiffRam succeeded in capturing all information of an *in situ* sample with clear distincting of both solid and liquid phase.

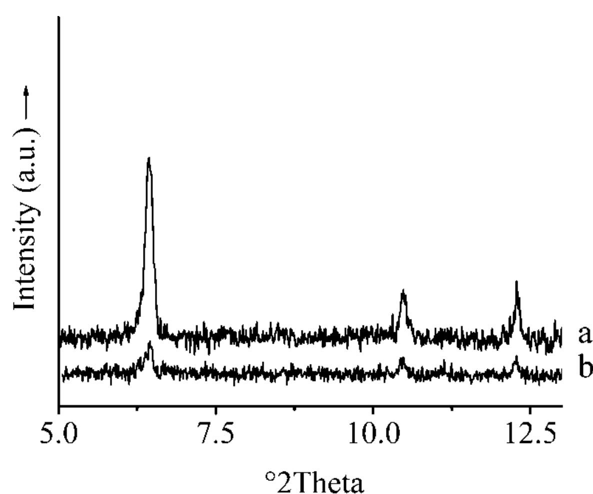

Fig. 8: XRD patterns of the hydrothermal condensation of Zeolite A at 4 h: separated sediment (a) and *in situ* sample containing both the solid and liquid phase (b) (Si/Al = 1).

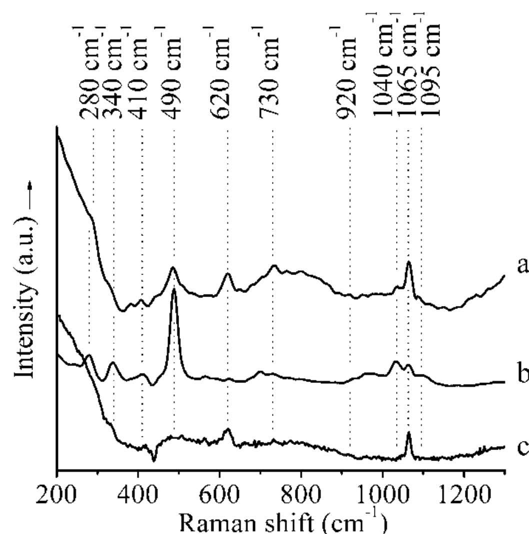

Fig. 9: UV-Raman investigation spectra of the hydrothermal condensation of Low-Silica zeolite A at 4 h *in situ* (a) and separated sediment (b) and liquid phase (c) (Si/Al = 1).

Crystal structure analysis of final zeolite X and A powders

The samples for X-ray powder diffraction (XRPD) were treated at 400 °C and sealed in a capillary at nitrogen atmosphere. Capillaries were measured on a STOE STADI MP with focusing monochromator (CuKα1) in Debye-Scherrer geometry with a position sensitive detector (6° 2θ) in a range between 3° and 67° 2θ and a resolution of 0.01° 2θ. Measurements occurred at room temperature. Rietveld refinement was performed with the GSAS software.[11]

Zeolite X

Analysis of the framework structure model for Zeolite X revealed that next to FAU small amount of LTA is present in the product (5% wt). The framework of Zeolite X was refined in Fig. 10 based on the publication of Porcher F. et al.[12] For the second phase that has LTA topology our Rietveld refinement results for Zeolite A were used. Rietveld refinement of Zeolite X confirmed FAU topology with sodium cations Na1 and Na2 in the framework close to two independent 6Rs positions of the sodalite cage occupied to 90 % for each position, Na3 in the supercage near the 12R with an occupancy 18 % and K in the supercage near the 12R with an occupancy 22.5 %. The final refinement led to satisfactory R values (R_p = 0.0557, R_{wp} = 0.0733, expected R_{exp} = 0.0195). Framework angles and bondlengths of Zeolite X are given in Table 1.

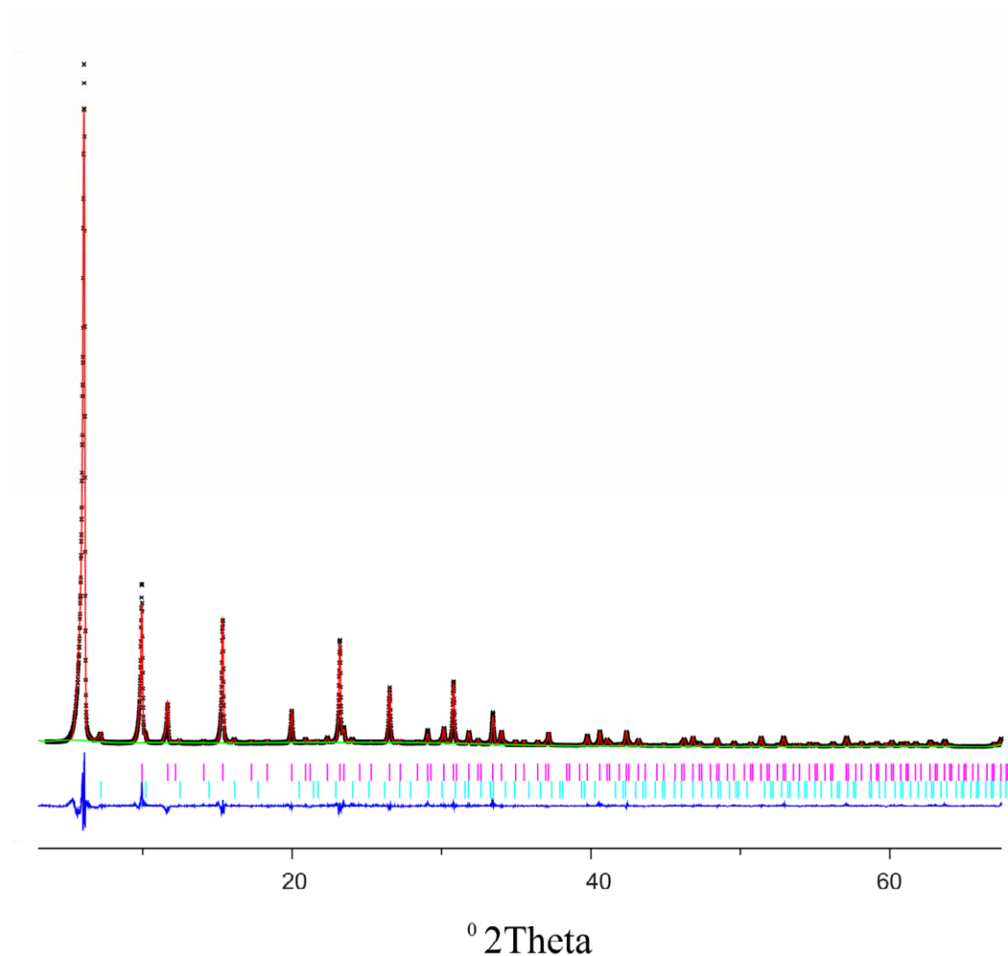

Fig. 10: Experimental and calculated patterns of the refined structure model for Zeolite X, the difference plot and the reflection markers for each phase.

Table 1: Framework angles and bondlengths of Zeolite X.

Vector	Length /Å
Si1_O1	1.58926(1)
Si1_O2	1.66430(1)
Si1_O3	1.62943(1)
Si1_O4	1.62758(1)
Average	1.54386

Vector	Length /Å
Al1_O1	1.82051(2)
Al1_O2	1.79809(2)
Al1_O3	1.74221(1)
Al1_O4	1.78946(1)
Average	1.78757

Angle	Degrees /°
Si1_O1_Al1	127.683(0)
Si1_O2_Al1	138.474(0)
Si1_O3_Al1	137.966(0)
Si1_O4_Al1	136.937(0)
Average	135.265

Angle	Degrees /°
O1_Si1_O2	120.814(1)
O1_Si1_O3	115.759(0)
O1_Si1_O4	100.432(0)
O2_Si1_O3	102.141(0)
O2_Si1_O4	99.291(0)
O3_Si1_O4	118.169(1)
Average	109.434

Angle	Degrees /°
O1_Al1_O2	112.811(0)
O1_Al1_O3	114.513(1)
O1_Al1_O4	104.275(0)
O2_Al1_O3	105.498(0)
O2_Al1_O4	103.633(1)
O3_Al1_O4	115.786(1)
Average	109.419

This journal is © The Owner Societies 2011

Zeolite A

The framework structure model for Zeolite A was refined based on the original publication of J.J. Pluth and J.V. Smith (Fig. 11).[13] Rietveld refinement confirmed LTA topology with sodium cations in the framework positions 6Rs occupied to 100 %, 8Rs occupied to 67 % and on site close to 4Rs in the large cage occupied to 17 %. At the final stage of the refinement 2 water positions were located on site close to 8Rs with occupancy 33 % and in plane 8Rs with occupancy 17.5 % that led to satisfactory R values (R_p = 0.0401, R_{wp} = 0.0543, expected R_{exp} = 0.0211). Framework angles and bondlengths of Zeolite A are given in Table 2.

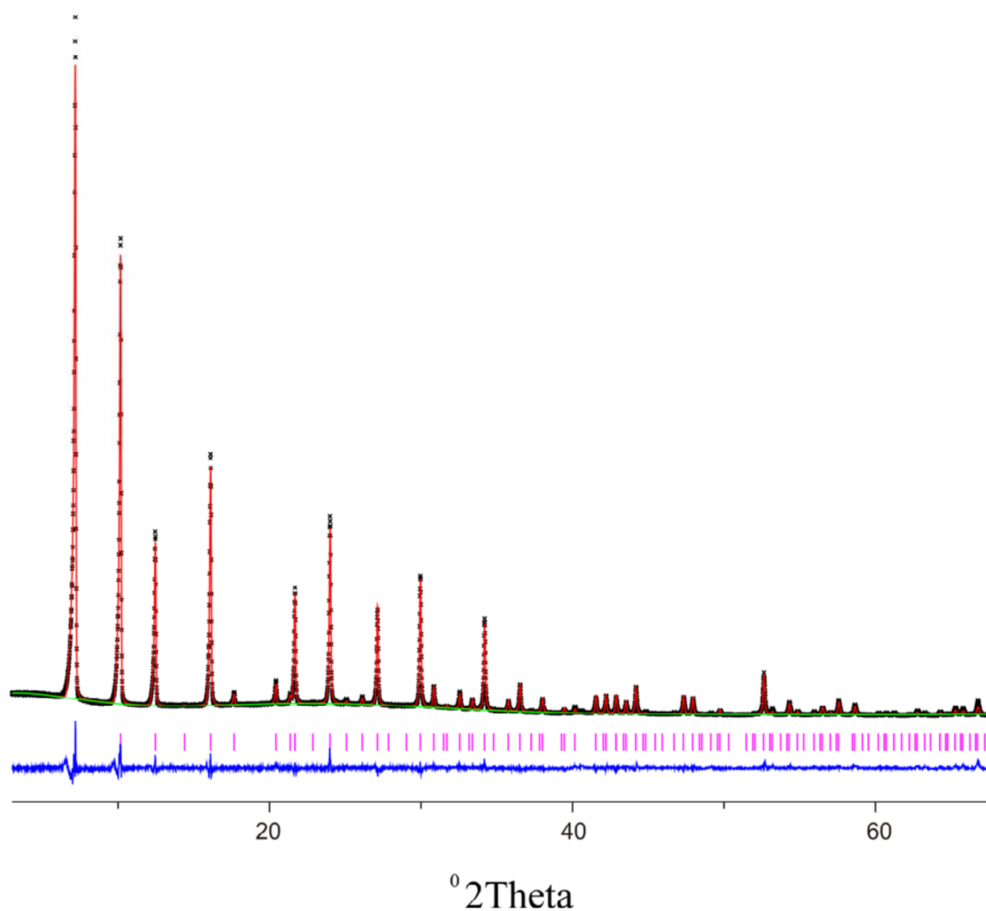

Fig. 11: Experimental and calculated patterns of the refined structure model for Zeolite A, the difference plot and the reflection markers.

Table 2: Framework angles and bondlengths of Zeolite A.

Vector	Length /Å
Si1_O1	1.576(24)
Si1_O2	1.611(23)
Si1_O3	1.635(14)
Si1_O3’	1.635(14)
Average	1.614

Vector	Length /Å
Al1_O1	1.686(24)
Al1_O2	1.689(23)
Al1_O3	1.716(14)
Al1_O3’	1.716(14)
Average	1.702

Angle	Degrees /°
Si1_O1_Al1	147.2(8)
Si1_O2_Al1	167.3(5)
Si1_O3_Al1	145.5(5)
Average	153.3

Angle	Degrees /°
O1_Si1_O2	114.0(10)
O1_Si1_O3	111.4(5)
O1_Si1_O3’	111.4(5)
O2_Si1_O3	105.7(6)
O2_Si1_O3’	105.7(6)
O3_Si1_O3’	108.2(7)
Average	109.4

Angle	Degrees /°
O1_Al1_O2	110.4(9)
O1_Al1_O3	110.7(5)
O1_Al1_O3’	110.7(5)
O2_Al1_O3	106.8(6)
O2_Al1_O3’	106.8(6)
O3_Al1_O3’	111.3(7)
Average	109.5

All necessary values for the refinement of Zeolite A and X are given in additional Zeolite A.cif and Zeolite X.cif files, respectively.

References

1. C. Bremard and M. Le Maire, *Journal of Physical Chemistry*, 1993, **97**, 9695-9702.
2. P. K. Dutta, K. M. Rao and J. Y. Park, *Journal of Physical Chemistry*, 1991, **95**, 6654-6656.
3. P. K. Dutta, D. C. Shieh and M. Puri, *Zeolites*, 1988, **8**, 306-309.
4. P. K. Dutta and J. Twu, *Journal of Physical Chemistry*, 1991, **95**, 2498-2501.
5. P.-P. Knops-Gerrits, D. E. De Vos, E. J. P. Feijen and P. A. Jacobs, *Microporous Materials*, 1997, **8**, 3-17.
6. Y. Yu, G. Xiong, C. Li and F. S. Xiao, *Microporous and Mesoporous Materials*, 2001, **46**, 23-34.
7. J. Twu, P. K. Dutta and C. T. Kresge, *Zeolites*, 1991, **11**, 672-679.
8. F. Roozeboom, H. E. Robson and S. S. Chan, *Zeolites*, 1983, **3**, 321-328.
9. F. T. Fan, Z. C. Feng, G. N. Li, K. J. Sun, P. F. Ying and C. Li, *Chemistry-a European Journal*, 2008, **14**, 5125-5129.
10. G. Xiong, Y. Yu, Z.-c. Feng, Q. Xin, F.-S. Xiao and C. Li, *Microporous and Mesoporous Materials*, 2001, **42**, 317-323.
11. A. Larson and R. Von Dreele, *Los Alamos National Laboratory Report LAUR*, 2004, 86 -748.
12. F. Porcher, M. Souhassou, Y. Dusausoy and C. Lecomte, *European Journal of Mineralogy*, 1999, **11**, 333-343.
13. J. J. Pluth and J. V. Smith, *Journal of the American Chemical Society*, 1980, **102**, 4704-4708.